

# Wavefront Reconstruction for Fractional Lateral Shear Measurements using Weighted Integer Shear Averages

Samia Heshmat<sup>a</sup>, Satoshi Tomioka<sup>b,\*</sup>, Naoki Miyamoto<sup>b</sup>, Yuji Yamauchi<sup>b</sup>, Yutaka Matsumoto<sup>b</sup>, Naoki Higashi<sup>b</sup>

<sup>a</sup>Faculty of Engineering, Aswan University, Aswan, 81542, Egypt

<sup>b</sup>Faculty of Engineering, Hokkaido University, Sapporo, 060-8628, Japan

---

## Abstract

Wavefront reconstruction in lateral shearing interferometry typically assumes that the shear amount is an integer multiple of the sampling interval. When the shear is fractional, approximating it with the nearest integer value leads to noticeable reconstruction errors. To address this, we propose a weighted integer shear averaging method. The approach combines reconstructions from nearby integer shears with carefully chosen weights designed to cancel the dominant error terms. Analytical error analysis shows that two-shear averaging removes first-order errors, while three-shear averaging removes second-order errors. Numerical simulations with a test wavefront confirm that the method achieves significantly lower RMS error than conventional single-shear reconstruction. The technique is simple, computationally efficient, and can be readily extended to two-dimensional interferometry. This makes weighted integer shear averaging a practical and accurate tool for wavefront reconstruction when fractional shear is unavoidable.

*Keywords:* Shear interferometry, Phase measurement, Wavefront reconstruction, Fractional shear.

---

## 1. Introduction

Interferometers are widely employed for wavefront measurement and optical metrology applications [1, 2, 3]. In conventional two-beam interferometers such as the Michelson or Mach-Zehnder configuration, the object beam and the reference beam travel along separate optical paths. This path separation makes such system highly sensitive to environmental disturbances such as vibrations, temperature gradients, and air turbulence, which are difficult to correct in practice [4, 5]. Moreover, because the beam must be split and recombined, numerous optical components are required, which further increases system complexity and susceptibility to noise sources.

For example, in certain measurement systems, such as a computed tomography (CT) or a tomographic phase microscopy, wavefront measurements are performed by changing the angle of incidence of the probing beam [6, 7, 8, 9]. In such cases, vibrations and misalignments from each optical element act independently, further complicating reliable interference measurements. In contrast, a shear interferometer offers a more robust approach, the object wavefront, after transmission or reflection from the object under test, is split into two parallel beams: the original object beam and a laterally displaced replica (the shear beam) [10, 11]. The two beams interfere with each other, sharing almost the same optical paths and requiring fewer optical elements than conventional two-beam interferometers, thereby mitigating environmental sensitivity and system complexity.

However, unlike the two-beam interferometers, the

fringes recorded in a shear interferometer encode only the wavefront difference between the two beams, rather than the absolute wavefront itself. Consequently, numerical processing is required to reconstruct the actual object wavefront from this differential measurement. Mathematically, the relationship between the measured differential phase  $f^M(x, s)$  for a lateral shear  $s$  and the original object wavefront  $\phi(x)$  can be expressed as

$$f^M(x, s) = \phi(x + s) - \phi(x). \quad (1)$$

The methods developed to address the wavefront reconstruction problem in lateral shearing interferometry can be broadly classified into modal and zonal approaches. The latter is further classified into two groups: approaches based on least-squares method in spatial domain, and approaches based on Fourier transform (FT).

In modal methods, the unknown wavefront  $\phi(x)$  is expanded using orthogonal basis functions, typically Zernike polynomials [12, 13, 14, 15, 16, 17, 18, 19]. These methods are robust against measurement noise but tend to smooth out high-frequency or localized wavefront variations.

In the zonal methods with least-squares method in the spatial domain [20, 21, 22, 23, 24], the reconstruction problem is formulated as a system of equations where the variables to be solved are wavefronts at the measured pixels. Solving the equations requires a large computational cost because the number of variables is large. Moreover, these methods suffer from rank-deficient problems. They can be solved by using multi-shear methods which employ two or more measurements of phase difference with different shear amounts.

In contrast, the zonal methods based on FT [25, 26], have no need to solve simultaneous equations, since it only requires a Fourier transform, multiplication by a factor, and an inverse Fourier transform; such as  $\phi(x) = \mathcal{F}^{-1}\{\mathcal{F}\{f^M(x; s)\}/(e^{iks} - 1)\}$  where  $\mathcal{F}\{\}$  means FT operator with the basis function  $e^{-ikx}$ .

However, FT-based reconstruction suffers from several inherent limitations regarding reconstruction errors. The first is the loss of the  $1/s$  harmonic components in the spectral domain. To address this problem, the use of the Tikhonov regularization [27], or multi-shears methods [28, 29] similar as the zonal methods based on least-squares in spatial domain, are proposed. The second major problem is that FT is based on periodic boundary, which introduces spectral leakage when the underlying phase is aperiodic. The natural extension technique proposed by Elster *et al.* [30, 31, 32] mitigates boundary artifacts by introducing mathematically consistent domain padding which has been applied to many applications [33, 34, 35, 36, 9].

Tomioka *et al.* [37] proposed a coupling method of the spectral interpolation method to solve the loss of  $1/s$  harmonics problem with the natural extension method to solve periodicity problem for one-dimensional reconstruction. This method requires only a single differential phase measurement in one dimension. For two-dimensional reconstruction, it also couples the least-squares method [38] to solve ambiguities of uniform wavefront called piston term. However, a limitation remains regarding shear amounts.

The basic principle of lateral shearing interferometry and most of the wavefront reconstruction methods assume that the shear applied during measurement is an integer multiple of the spatial sampling interval  $\delta_x$ . However, in real-world systems, it is often impractical to constrain shear values to discrete grid-aligned steps. Limitations in mechanical or electronic control, or the need for higher resolution, frequently result in the application of non-integer (fractional) shears. This mismatch introduces a significant challenge. In this manuscript, we provide a detailed theoretical analysis of the wavefront reconstruction errors, deriving expressions for the reconstruction error introduced by using a nearby integer shear instead of the true fractional value. The error can be represented as a series expansion in terms of the normalized shear difference, with leading terms that are proportional to the first and second powers of the deviation. Furthermore, we build upon that theoretical foundation to develop a practical method to reduce the reconstruction error in fractional shear measurements.

This manuscript is structured as follows. Section 2 reviews the shear interference fringe analysis process. Section 3 summarizes the analytical error expressions for fractional shear substitution. In addition, this section introduces the proposed multiple integer shear averaging approach and provides the mathematical basis for its effectiveness. Section 4 presents numerical simulations validating the proposed approach, and Section 5 concludes with a discussion of future directions.

## 2. Shear interference fringe analysis process

Unlike a conventional two-beam interferometer that compares an object wavefront with a separate reference beam, a shear interferometer laterally displaces the object

beam itself to generate interference. Consequently, the recorded fringes represent the phase difference between two laterally shifted replicas of the same wavefront rather than the absolute phase distribution. This makes direct interpretation of the measured intensity pattern nontrivial and necessitates numerical reconstruction to recover the original wavefront. The measured fringe pattern  $I^M(\mathbf{r}; \mathbf{s})$  in the lateral shear interferometry with a shear amount  $\mathbf{s}$  can be simply expressed as

$$I^M(\mathbf{r}; \mathbf{s}) = I_0(\mathbf{r}) [1 + \cos(\mathbf{k}_{\text{bg}} \cdot \mathbf{r} + \delta\phi(\mathbf{r}; \mathbf{s}))], \quad (2)$$

where  $\mathbf{k}_{\text{bg}}$  denotes the spatial carrier frequency determined by the difference between wavenumber vectors in vacuum of the two beams as  $\mathbf{k}_{\text{bg}} = \mathbf{k}_0(\mathbf{r} + \mathbf{s}) - \mathbf{k}_0(\mathbf{r})$  which is almost uniform; and  $\delta\phi(\mathbf{r}; \mathbf{s})$  represents the phase difference between the two beams represented as

$$\delta\phi(\mathbf{r}; \mathbf{s}) = \phi(\mathbf{r} + \mathbf{s}) - \phi(\mathbf{r}). \quad (3)$$

Thus, shear interferometry provides phase differences that require specialized reconstruction algorithms, which are the main focus of this study. Eq. (2) means that the parallel stripes are distorted by non-uniform  $\delta\phi(\mathbf{r}; \mathbf{s})$ . Once  $I^M(\mathbf{r}; \mathbf{s})$  is obtained through a measurement,  $e^{j\delta\phi(\mathbf{r}; \mathbf{s})}$  can be extracted in the same way as a two-beam interferometer by the Fourier-transform method [39], after that the phase difference can be obtained by taking a complex argument; however, the obtained phase is a wrapped phase including  $2\pi$  phase jumps.

$$\mathcal{W}\{\delta\phi(\mathbf{r}; \mathbf{s})\} = \arg\left\{I_0(\mathbf{r})e^{j\delta\phi(\mathbf{r}; \mathbf{s})}\right\}, \quad (4)$$

where  $\mathcal{W}\{\}$  shows the wrapping operator. To solve the phase jump problem, a phase unwrapping process, which is the same as the case of two-beam interferometer, must be applied. Several unwrapping methods have been proposed; among them the localized compensator phase unwrapping method [40] has demonstrated superior performance [41]. The unwrapped phase can then be expressed as

$$f^M(\mathbf{r}; \mathbf{s}) = \mathcal{U}\{\mathcal{W}\{\delta\phi(\mathbf{r}; \mathbf{s})\}\}, \quad (5)$$

where  $\mathcal{U}\{\}$  shows the unwrapping operator, and the superscript ‘M’ means quantities obtained from measured fringe  $I^M(\mathbf{r}; \mathbf{s})$  through the aforementioned processes.

In practice, two-dimensional reconstruction is frequently reformulated into one-dimensional differential equations, where the wavefront  $\phi(x)$  is recovered from the measured shear data  $f^M(x; s)$  defined in (1). This reduction improves computational efficiency but introduces independent piston offsets along each shear direction. Since the piston term problem to reconstruct a two-dimensional wavefront can be solved by coupling with the method proposed by Tian *et al.* [38], we focus on one-dimensional reconstruction in the following.

If the shear during measurement is an integer shear ( $s = S$ ), the same shear amount  $S$  can be used, so it holds:

$$\phi_{S;S}(x) = \text{Rec}\{f^M(x, S); S\} = \phi(x), \quad (6)$$

where the  $\text{Rec}\{\}$  operator represents reconstruction operator to obtain the phase from the measured phase difference;

and the first and second arguments express the difference phase to be applied the operator and the integer shear used for the reconstruction, respectively. When we employ the spectral interpolation method [37] for  $\text{Rec}\{\}$ , the reconstructed phase includes errors due to shear harmonics of  $\phi(x)$ , but we choose  $s$  such that this is negligible, and we consider the errors to be negligible. On the other hand, if the shear during measurement is non-integer,

$$\phi_{s;S}(x) = \text{Rec}\{f^M(x, s); S\} \neq \phi(x). \quad (7)$$

Since  $s$  and  $S$  differ, the reconstructed wavefront  $\phi_{s;S}(x)$  contains significant error relative to the original wavefront  $\phi(x)$ .

### 3. Dominant error reduction using multiple integer-shear averaging

To mitigate reconstruction errors arising from fractional shear measurements, we introduce a weighted integer shear averaging method. The core idea is to suppress the dominant error components present in  $\phi_{s;S}(x)$  by utilizing the properties of integer shear substitutions. To clarify the numerical reconstruction from fractional-shear measurements, we first define  $\phi_{s;S}^\dagger(x)$  as the scaled integer-shear approximation of the wavefront, obtained by substituting the fractional shear  $s$  with a nearby integer shear  $S$ . This reconstructed function preserves the global structure of the true wavefront but generally contains residual error components whose amplitude depends on the difference between the fractional shear and the integer shear. The key observation underlying the proposed method is that when several symmetric integer shears with  $S_q$ , where  $q$  can be, for example  $\{1, 2\}$ , are selected around  $s$ , their corresponding reconstructions  $\phi_{s;S_q}^\dagger(x)$  exhibit dominant error components with opposite phases. Therefore, by averaging these wavefronts, the leading error terms are canceled while the true wavefront contribution is retained. In the subsections that follow, we first analyze the reconstruction errors produced when a single integer shear is used, and then demonstrate how these errors can be reduced by systematically averaging reconstructions obtained from several integer shears,  $S_q$ , located near the target fractional shear,  $s$ .

#### 3.1. Reconstruction error using a single integer shear

By expanding  $\phi(x + s)$  in the right-hand side of Eq. (1) using a Taylor series, integrating both sides, and rearranging terms, we obtain an expression for  $\phi(x)$  in terms of the differential wavefront:

$$\phi(x) = \frac{1}{s} \int f^M(x, s) dx - \sum_{n=1}^{\infty} \frac{s^n}{(n+1)!} \phi^{(n)}(x). \quad (8)$$

When the shear amount  $s$  is non-integer, the FT-based reconstruction techniques, such as the natural extension and spectral interpolation methods, cannot directly handle the fractional shear. In such cases,  $s$  is typically replaced by a nearby integer shear  $S$ , which inevitably introduces approximation errors in the reconstructed wavefront.

The difference between the fractional shear and the integer shear is denoted by  $\epsilon$  as

$$\epsilon \equiv S - s. \quad (9)$$

When the wavefront is reconstructed using the integer shear  $S$ , the observed quantity  $f^M(x, s)$  still depends on the original fractional shear  $s$ . However, in Eq. (8), both  $s$  in the factor in the first term and  $s$  in the second term are replaced by  $S$ . Thus, the wavefront is reconstructed as follows:

$$\phi_{s;S}(x) = \frac{1}{S} \int f^M(x, s) dx - \sum_{n=1}^{\infty} \frac{S^n}{(n+1)!} \phi_{s;S}^{(n)}(x). \quad (10)$$

For both Eqs. (8) and (10), if the second term on the right-hand sides are sufficiently smaller than the first term, then dominant contribution comes from the integral. From the comparisons of the first terms, we obtain the relation between  $\phi(x)$  and  $\phi_{s;S}(x)$  given by

$$\phi(x) \simeq \frac{S}{s} \phi_{s;S}(x) \equiv \phi_{s;S}^\dagger(x). \quad (11)$$

This expression indicates that the reconstructed wavefront  $\phi_{s;S}(x)$  using the integer shear  $S$  instead of the fractional shear  $s$  that should originally be used for evaluation is approximately equal to  $\phi(x)$  scaled by a factor of  $s/S$ . For instance, if  $s = 1.5$  and  $S = 1$ , the resulting error would be about 50%, which is generally unacceptable. In other words, the scaled wavefront  $\phi_{s;S}^\dagger(x)$  can reduce the error in the first integral in Eq. (10). The residual error,  $d_{s;S}^\dagger(x)$  in this approximation for  $\phi(x)$  defined by

$$d_{s;S}^\dagger(x) \equiv \phi_{s;S}^\dagger(x) - \phi(x) \quad (12)$$

will be evaluated later; however, its exact expression is expected to be complicated, involving nested summations. To make this more practical, an approximated form  $\phi_{s;S}^{\dagger*}(x)$  instead of  $\phi_{s;S}^\dagger(x)$  will be introduced and its error will be analyzed. The  $n$ -th derivatives of  $\phi(x)$  are approximated as  $\phi^{(n)}(x) \simeq \phi_{s;S}^{\dagger(n)}(x)$  from Eq. (11). By using this approximation, the approximated phase  $\phi_{s;S}^{\dagger*}(x)$  is defined from  $\phi_{s;S}^\dagger(x)$  as follows.

$$\begin{aligned} \phi_{s;S}^{\dagger*}(x) &= \frac{1}{s} \int f^M(x, s) dx - \sum_{n=1}^{\infty} \frac{S^n}{(n+1)!} \frac{S}{s} \phi_{s;S}^{(n)}(x) \\ &= \frac{1}{s} \int f^M(x, s) dx - \sum_{n=1}^{\infty} \frac{S^n}{(n+1)!} \phi_{s;S}^{\dagger(n)}(x) \\ &\simeq \frac{1}{s} \int f^M(x, s) dx - \sum_{n=1}^{\infty} \frac{S^n}{(n+1)!} \phi^{(n)}(x) \\ &\equiv \phi_{s;S}^{\dagger*}(x). \end{aligned} \quad (13)$$

Comparing  $\phi_{s;S}^{\dagger*}(x)$  with  $\phi(x)$  in Eq. (8), the only difference is that  $s$  in the second term is replaced with  $S$ . The

difference is evaluated as

$$\begin{aligned}
d_{s;S}^{\dagger*}(x) &\equiv \phi_{s;S}^{\dagger*}(x) - \phi(x) \\
&= \sum_{n=1}^{\infty} \frac{-1}{(n+1)!} (S^n - s^n) \phi^{(n)}(x) \\
&= \sum_{n=1}^{\infty} \frac{-1}{(n+1)!} ((1+\hat{\epsilon})^n - 1) \hat{\phi}^{(n)}(x), \quad (14) \\
\hat{\epsilon} &\equiv \frac{\epsilon}{s} = \frac{S-s}{s}, \\
\hat{\phi}^{(n)}(x) &\equiv \frac{d^n \phi(x)}{d(x/s)^n} = s^n \phi^{(n)}(x), \quad (15)
\end{aligned}$$

where  $\hat{\epsilon}$  and  $\hat{\phi}^{(n)}$  in  $\hat{\phi}^{(n)}(x)$  represent the quantities by which  $x$ -axis is normalized by  $s$ ;  $\hat{\phi}^{(n)}(x)$  has the same dimension as  $\phi(x)$ . The factor  $(1+\hat{\epsilon})^n - 1$  on the right-hand side of Eq. (14) can be expressed by a binomial theorem expansion as

$$(1+\hat{\epsilon})^n - 1 = \sum_{m=1}^n \frac{n!}{m!(n-m)!} \hat{\epsilon}^m. \quad (16)$$

The summation of infinite terms of  $n$  on the right-hand side in Eq. (14) and the summation of the finite terms of  $m$  from the binomial expansion is expressed as a double summation of  $n$  and  $m$ . If we exchange the order of the loop integers  $n$  and  $m$  in the double summation and put  $l = n - m + 1$  ( $n = l + m - 1$ ),

$$\begin{aligned}
\sum_{n=1}^{\infty} \sum_{m=1}^n a_n b_m &= \sum_{m=1}^{\infty} \sum_{n=m}^{\infty} a_n b_m \\
&= \sum_{m=1}^{\infty} \sum_{l=1}^{\infty} a_{l-m+1} b_m = \sum_{(m,l) \in \mathbb{N}^2} a_{l-m+1} b_m. \quad (17)
\end{aligned}$$

Thus, the domains of  $m$  and  $l$  are all natural numbers. Therefore,  $d_{s;S}^{\dagger*}(x)$  is

$$\begin{aligned}
d_{s;S}^{\dagger*}(x) &= \sum_{(m,l) \in \mathbb{N}^2} \alpha_{l,m}^* \hat{\phi}^{(l+m-1)}(x) \hat{\epsilon}^m \\
&= \sum_{m \in \mathbb{N}} \hat{A}_m^*(x) \hat{\epsilon}^m. \quad (18)
\end{aligned}$$

where

$$\alpha_{l,m}^* \equiv \frac{-1}{(l+m)! m! (l-1)!}, \quad (19)$$

$$\hat{A}_m^*(x) \equiv \sum_{l \in \mathbb{N}} \alpha_{l,m}^* \hat{\phi}^{(l+m-1)}(x). \quad (20)$$

Eq. (18) shows that the error of  $\phi_{s;S}^{\dagger*}(x)$  is given by a power series of  $\hat{\epsilon}$ . Except for special cases ( $|s| < \delta_x/2$ ),  $|\hat{\epsilon}| \leq 1/2$ , and since  $|\hat{\epsilon}| > |\hat{\epsilon}|^m$  ( $m > 1$ ), this dominant term is the first-order term  $\hat{A}_1^*(x)\hat{\epsilon}$ , which is proportional to  $\hat{\epsilon}$ . Furthermore, if we assume that the term containing the first derivative  $\phi^{(1)}(x)$  is dominant among the terms of  $\hat{A}_1^*(x)$  defined by Eq. (20), then the magnitude of the error is reduced as  $|d_{s;S}^{\dagger*}(x)| \sim |\hat{\epsilon}\hat{\phi}^{(1)}(x)/2| = |\epsilon\phi^{(1)}(x)/2|$ , in which the dependency of  $s$  does not appeared explicitly. In other words, under these conditions, when choosing  $S$  in the vicinity of  $s$ , for any  $s$ , the error is proportional only to  $\epsilon$ , which is  $s - S$ .

The aforementioned  $\phi_{s;S}^{\dagger*}(x)$  is the approximation of  $\phi_{s;S}^{\dagger}(x)$  in order to roughly evaluate the nature of error. In the remaining part of this subsection, we will evaluate the error of  $\phi_{s;S}^{\dagger}(x)$  more precisely. In general, the error increases as  $\hat{\epsilon}$  increases; therefore, it is natural to assume that  $d_{s;S}^{\dagger}(x)$  is also given by the power series expansion of  $\hat{\epsilon}$ , similar to  $d_{s;S}^{\dagger*}(x)$  in Eq. (18). However, since we cannot reject the possibility that uniform errors remain, we include  $\hat{\epsilon}^0$  in the expansion.

$$d_{s;S}^{\dagger}(x) = \sum_{m \in \{0,1,2,\dots\}} \hat{A}_m(x) \hat{\epsilon}^m. \quad (21)$$

The difference between Eqs. (10) and (8) is only the difference between the second terms of each equation, which are  $S^n \phi_{s;S}^{\dagger(n)}(x)$  and  $s^n \phi^{(n)}(x)$ . The difference of them is expressed as follows:

$$\begin{aligned}
S^n \phi_{s;S}^{\dagger(n)}(x) - s^n \phi^{(n)}(x) &= (1+\hat{\epsilon})^n \left[ \hat{\phi}^{(n)}(x) + \hat{d}_{s;S}^{\dagger(n)}(x) \right] - \hat{\phi}^{(n)}(x) \\
&= ((1+\hat{\epsilon})^n - 1) \left[ \hat{\phi}^{(n)}(x) + \hat{d}_{s;S}^{\dagger(n)}(x) \right] + \hat{d}_{s;S}^{\dagger(n)}(x). \quad (22)
\end{aligned}$$

Then, the factor of the first term on the right-hand side can be transformed in the same way as the derivation of Eq. (14) to Eq. (18), and the difference  $\hat{d}_{s;S}^{\dagger}(x)$  becomes

$$\begin{aligned}
\hat{d}_{s;S}^{\dagger}(x) &= \sum_{(m,l) \in \mathbb{N}^2} \alpha_{l,m}^* \left[ \hat{\phi}^{(l+m-1)}(x) + \hat{d}_{s;S}^{\dagger(l+m-1)}(x) \right] \hat{\epsilon}^m \\
&\quad + \sum_{n \in \mathbb{N}} \beta_n \hat{d}_{s;S}^{\dagger(n)}(x), \quad (23)
\end{aligned}$$

$$\beta_n \equiv \frac{-1}{(n+1)!}. \quad (24)$$

The difference between  $\hat{d}_{s;S}^{\dagger}(x)$  in Eq. (23) and  $d_{s;S}^{\dagger*}(x)$  in Eq. (18) is whether the derivatives of  $\hat{d}_{s;S}^{\dagger}(x)$  are included. To evaluate  $\hat{\epsilon}$ -dependency of  $\hat{d}_{s;S}^{\dagger}(x)$ , we must evaluate dominant term of the right-hand side. The dominant term of the first term is the first order of  $\hat{\epsilon}$  because  $|\hat{\epsilon}| < 1$ . However, the dominant term in the last term is unknown from the form of Eq. (23) because the nature of the derivatives,  $\hat{d}_{s;S}^{\dagger(n)}(x)$  is unknown. The derivatives are expressed as a recursive form by taking differentiation of Eq. (23).

$$\begin{aligned}
\hat{d}_{s;S}^{\dagger(p)}(x) &= \sum_{(m,l) \in \mathbb{N}^2} \alpha_{l,m}^* \left[ \hat{\phi}^{(p+l+m-1)}(x) + \hat{d}_{s;S}^{\dagger(p+l+m-1)}(x) \right] \hat{\epsilon}^m \\
&\quad + \sum_{n \in \mathbb{N}} \beta_n \hat{d}_{s;S}^{\dagger(p+n)}(x), \quad (25)
\end{aligned}$$

where we applied  $\hat{d}_{s;S}^{\dagger(0)}(x) = d_{s;S}^{\dagger}(x)$  from Eq. (15) with  $p = 0$ . To examine the nature of  $\hat{d}_{s;S}^{\dagger}(x)$ , we first evaluate the zeroth order term of  $\hat{\epsilon}$ , since it may become a larger term than the first order term. The minimum order of  $\hat{\epsilon}$  in the first term on the right-hand side of Eq. (23) is the first order of  $\hat{\epsilon}$  as mentioned above; therefore, the zeroth order is only included in higher order derivatives of  $\hat{d}_{s;S}^{\dagger}(x)$  at the last term. The derivative shown in Eq. (25) also includes

the zeroth order term only at the last term. When we evaluate it sequentially, we obtain the zeroth order term  $\hat{A}_0(x)$  as

$$\hat{A}_0(x) = \sum_{(n,n',n'',\dots) \in \mathbb{N}^\infty} \beta_n \beta_{n'} \beta_{n''} \dots \hat{d}_{s;S}^{\dagger(n+n'+n''+\dots)}(x) \quad (26)$$

$$= \sum_{n \in \mathbb{N}^\infty} \left( \prod_{i \in \mathbb{N}} \beta_{n_i} \right) \hat{d}_{s;S}^{\dagger(\sum_i n_i)}(x). \quad (27)$$

If the derivative of  $\hat{d}_{s;S}^{\dagger(\infty)}(x)$  is finite, then  $\hat{A}_0(x) = 0$  because  $\beta_{n_i} < 1$  and the factor  $\prod_{i \in \mathbb{N}} \beta_{n_i} = 0$ . In other words, the minimum order of  $\hat{d}_{s;S}^{\dagger}(x)$  is the first order, as well as  $\hat{d}_{s;S}^{\dagger*}(x)$ . Therefore, the power series expression of  $\hat{d}_{s;S}^{\dagger}(x)$  shown in Eq. (21) is modified as

$$\hat{d}_{s;S}^{\dagger}(x) = \sum_{m \in \mathbb{N}} \hat{A}_m(x) \hat{\epsilon}^m. \quad (28)$$

It should be noticed that  $\hat{A}_m(x)$  is independent of  $\hat{\epsilon}$  or  $S-s$ . By evaluating the derivative of this equation with respect to  $x$ , we obtain

$$\hat{d}_{s;S}^{\dagger(p)}(x) = \sum_{m \in \mathbb{N}} \hat{A}_m^{(p)}(x) \hat{\epsilon}^m. \quad (29)$$

The minimum order of  $\hat{\epsilon}$  is also 1 for the derivatives. Substituting this equation into Eq. (23) and expressing the derivatives with summation by Eq. (20), we obtain the following form.

$$\begin{aligned} \hat{d}_{s;S}^{\dagger}(x) &= \sum_{m \in \mathbb{N}} \hat{A}_m \hat{\epsilon}^m + \sum_{(m,l,m') \in \mathbb{N}^3} \alpha_{l,m}^* \hat{A}_{m'}^{(l+m-1)}(x) \hat{\epsilon}^{m+m'} \\ &+ \sum_{(n,m) \in \mathbb{N}^2} \beta_n \hat{A}_m^{(n)}(x) \hat{\epsilon}^m. \end{aligned} \quad (30)$$

Let us consider the  $\hat{\epsilon}$ -dependency from this form. Regarding the first order coefficient function,  $\hat{A}_1(x)$ , since  $m+m' > 1$ , the second term on the right-hand side does not include the first order of  $\hat{\epsilon}$ , the terms including the first order are found on the first and the last term.

$$\hat{A}_1(x) = \hat{A}_1^*(x) + \sum_{n \in \mathbb{N}} \beta_n \hat{A}_1^{(n)}(x). \quad (31)$$

Taking a derivative of this equation to obtain a derivatives, and substituting the obtained derivative into the second term on the right-hand side of the above equation,  $\hat{A}_1^{(n)}(x)$  in the second term on the right-hand side is replaced by  $\hat{A}_1^{*(n)}(x)$  and the additional term with a double summation as

$$\begin{aligned} \hat{A}_1(x) &= \hat{A}_1^*(x) + \sum_{n \in \mathbb{N}} \beta_n \hat{A}_1^{*(n)}(x) \\ &+ \sum_{(n,n') \in \mathbb{N}^2} \beta_n \beta_{n'} \hat{A}_1^{(n+n')}(x). \end{aligned} \quad (32)$$

Similarly, by repeating this procedure, triple, quadruple, and more multiple summations appear in the last term. The order of derivatives in the terms added to the last term is higher than that of the preceding terms. Since the minimum differential order of  $\hat{A}_1^{*(n)}(x)$  is  $n+1$  due to Eq. (20), the first term on the right-hand side is dominant, if it can be assumed that the first-order derivative is smaller than the higher-order derivatives. Therefore,  $\hat{A}_1(x) \simeq \hat{A}_1^*(x)$ , then the properties of  $\hat{d}_{s;S}^{\dagger}(x)$  and  $\hat{d}_{s;S}^{\dagger*}(x)$  are the same.

### 3.2. Reconstruction using two integer shears

In subsection 3.1, we calculated  $\phi_{s;S}(x)$  by selecting a nearby integer shear  $S$  from the measured difference wavefront  $f^M(x, s)$  with a non-integer shear  $s$ . We then evaluated the error of the scaled  $\phi_{s;S}^{\dagger}(x)$ . Since the calculation is analytical, it is possible to change  $S$ , and the errors are different. By choosing two  $S_1$  and  $S_2$  as  $\phi_{s;S}^{\dagger}(x)$ , we obtain two equations whose respective errors are expressed as power series expansions shown in Eq. (28). By combining these two equations, we can eliminate any single term in the power series expansion. If the term to be eliminated is the most dominant first order term, the order of the remaining error will be reduced to the second order. In order to evaluate the residual error, the error model is expressed as a second-order power series expansion.

$$\begin{aligned} \phi_{s;S_q}^{\dagger}(x) - \phi(x) &= \hat{A}_1(x) \hat{\epsilon}_q + \hat{A}_2(x) \hat{\epsilon}_q^2 \\ &+ O(\hat{\epsilon}_q^3), \quad (q = \{1, 2\}). \end{aligned} \quad (33)$$

By multiplying the equations for  $q=1$  and  $q=2$  by  $\hat{\epsilon}_2$  and  $\hat{\epsilon}_1$ , respectively, and subtracting them, we can eliminate the terms containing  $\hat{A}_1(x)$ . Rearranging the result, we obtain an interpolated function between  $\phi_{s;S_1}^{\dagger}(x)$  and  $\phi_{s;S_2}^{\dagger}(x)$  as

$$\phi_{s;S_2}^{\dagger}(x) - \phi(x) = -\hat{A}_2(x) \hat{\epsilon}_1 \hat{\epsilon}_2 + O(\hat{\epsilon}_{1,2}^3), \quad (34)$$

$$\phi_{s;S_2}^{\dagger}(x) \equiv w_{S_2}^{(1)} \phi_{s;S_1}^{\dagger}(x) + w_{S_2}^{(2)} \phi_{s;S_2}^{\dagger}(x), \quad (35)$$

$$\begin{pmatrix} w_{S_2}^{(1)} \\ w_{S_2}^{(2)} \end{pmatrix} \equiv \frac{1}{\hat{\epsilon}_2 - \hat{\epsilon}_1} \begin{pmatrix} +\hat{\epsilon}_2 \\ -\hat{\epsilon}_1 \end{pmatrix}. \quad (36)$$

Let  $S_1$  and  $S_2$  be integer shears close to the fractional shear  $s$ , and let  $S_2 - S_1 = \epsilon_2 - \epsilon_1 = \delta_x$ , where  $\delta_x$  represents the sampling interval of the measured phase difference. The dependency of  $\hat{\epsilon}_1$  and  $\hat{\epsilon}_2$  in the first term on the right-hand side of Eq. (34) is

$$-\hat{\epsilon}_1 \hat{\epsilon}_2 = -\frac{\epsilon_1}{s} \frac{\epsilon_1 + \delta_x}{s} = \frac{1}{s^2} \left[ -\left( \epsilon_1 + \frac{\delta_x}{2} \right)^2 + \frac{\delta_x^2}{4} \right]. \quad (37)$$

We can see that the error is a quadratic function and becomes 0 at  $\epsilon_1 = 0, \delta_x$ , and has the maximum at  $\epsilon_1 = -\delta_x/2$  ( $\epsilon_2 = \delta_x/2$ ). As for  $s$ -dependency, since the derivative of  $\phi(x)$  contained in  $\hat{A}_2(x)$  is second or higher, if we assume that the terms containing second-order derivatives are more dominant than the terms containing third or higher ones. Furthermore, by using  $\hat{\phi}^{(2)}(x) = s^2 \phi^{(2)}(x)$  which is derived from Eq. (15), the factor  $1/s^2$  in the right-hand side of Eq. (37) is canceled, the  $s$ -dependency appears only in the term of  $\hat{\epsilon}_q^2$ .

### 3.3. Reconstruction using three integer shears

In the case of three integer shears  $S_q$  ( $q = \{1, 2, 3\}$ ), we can reduce two dominant error terms related to the first and the second order of  $\hat{\epsilon}$ . Similarly to the case of two shears, the model of the error is represented by the power series up to the third order to evaluate the remaining error.

$$\begin{aligned} \phi_{s;S_q}^{\dagger}(x) - \phi(x) &= \hat{A}_1(x) \hat{\epsilon}_q + \hat{A}_2(x) \hat{\epsilon}_q^2 + \hat{A}_3(x) \hat{\epsilon}_q^3 \\ &+ O(\hat{\epsilon}_q^4), \quad (q = \{1, 2, 3\}). \end{aligned} \quad (38)$$

From these, eliminating terms including  $\hat{A}_1(x)$  and  $\hat{A}_2(x)$ , we obtain

$$\phi_{s;S^3}^\dagger(x) - \phi(x) = -\hat{A}_3(x)\hat{\epsilon}_1\hat{\epsilon}_2\hat{\epsilon}_3 + O(\hat{\epsilon}_{1,2,3}^4), \quad (39)$$

$$\phi_{s;S^3}^\dagger(x) \equiv \sum_{q=1}^3 w_{S^3}^{(q)} \phi_q^\dagger, \quad (40)$$

$$\begin{pmatrix} w_{S^3}^{(1)} \\ w_{S^3}^{(2)} \\ w_{S^3}^{(3)} \end{pmatrix} = \frac{-1}{\Delta_\epsilon^3} \begin{pmatrix} \hat{\epsilon}_2\hat{\epsilon}_3(\hat{\epsilon}_3 - \hat{\epsilon}_2) \\ \hat{\epsilon}_3\hat{\epsilon}_1(\hat{\epsilon}_1 - \hat{\epsilon}_3) \\ \hat{\epsilon}_1\hat{\epsilon}_2(\hat{\epsilon}_2 - \hat{\epsilon}_1) \end{pmatrix}, \quad (41)$$

$$\Delta_\epsilon^3 \equiv (\hat{\epsilon}_3 - \hat{\epsilon}_2)(\hat{\epsilon}_2 - \hat{\epsilon}_1)(\hat{\epsilon}_1 - \hat{\epsilon}_3). \quad (42)$$

Let the integer shears  $S_q$  ( $q = \{1, 2, 3\}$ ) be arranged in order at equal intervals of  $\delta_x$ .

$$S_1 + \delta_x = S_2 = S_3 - \delta_x, \quad (43)$$

$$\epsilon_1 + \delta_x = \epsilon_2 = \epsilon_3 - \delta_x. \quad (44)$$

In this case, the error factor  $\hat{\epsilon}_1\hat{\epsilon}_2\hat{\epsilon}_3$  is

$$-\hat{\epsilon}_1\hat{\epsilon}_2\hat{\epsilon}_3 = \frac{1}{s^3}\epsilon_2(\delta_x^2 - \epsilon_2^2), \quad (45)$$

and is 0 at  $\epsilon_2 = 0, \pm\delta_x$ , and has the extreme values at  $\epsilon_2 = \pm\delta_x/\sqrt{3}$ . As for the dependence on  $s$ , as in subsections 3.1 and 3.2, if the term containing the third derivative is larger than the term containing the fourth derivative, then the factor  $1/s^3$  is canceled, and the  $s$ -dependency appears only as  $\epsilon_2^2$ .

In this section, the error reduction by the weighted average method which employs two or three scaled reconstructed wavefronts with integer shears were shown. If further error reduction is required, it can be extended to use four or more reconstructed wavefronts in similar ways.

#### 4. Numerical Simulations

To assess the applicability of the proposed method, we consider a representative case in which the true wavefront is known. This enables a quantitative evaluation of the reconstruction accuracy. As the representative example, we selected the following phase modulated sinusoidally, which is considered to be a little more complicated than the actual object.

$$\phi^{\text{True}}(x) = \exp\left(-\frac{(x-x_c)^2}{w^2}\right) \cos(k_0x) \quad (46)$$

$(k_0 = 2\pi/L).$

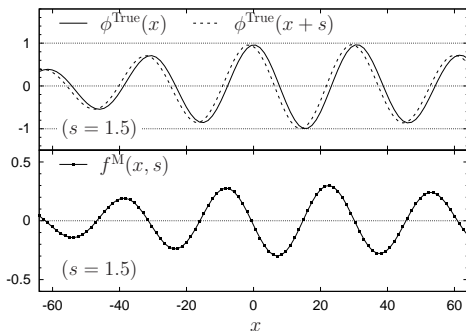


Figure 1: The simulation data as true wavefront  $\phi^{\text{True}}(x)$  and differential phase  $f^{\text{M}}(x, s)$  for  $s = 1.5$ .

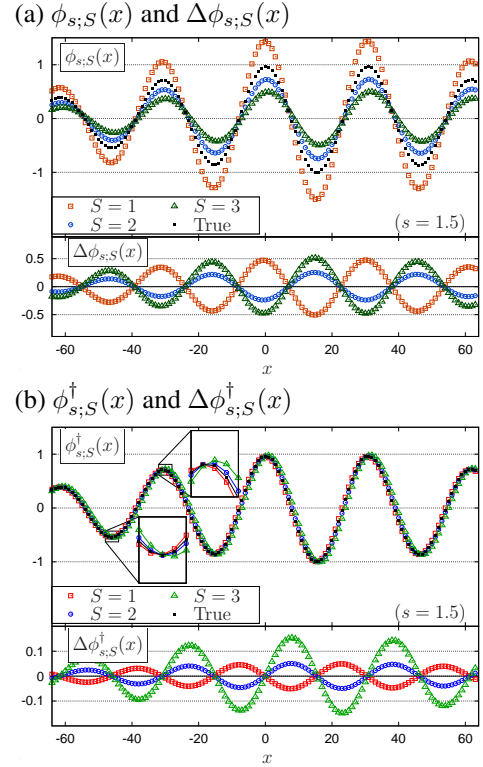


Figure 2: Comparisons of errors between the wavefront without and with scaling: (a) Reconstructed wavefronts by the basic method without scaling,  $\phi_{s;S}(x)$  and their errors,  $\Delta\phi_{s;S}(x) \equiv \phi_{s;S} - \phi^{\text{True}}(x)$ . (b) Scaled wavefronts,  $\phi_{s;S}^\dagger(x) = \frac{S}{s}\phi_{s;S}(x)$  and their errors,  $\Delta\phi_{s;S}^\dagger(x)$ . Note: The errors range in the lower panels differ between subfigures (a) and (b).

The true wavefront is specified by setting the parameters to  $(x_c, w, L) = (16, 50, 30)$ . Figure 1 shows the true wavefront together with the simulated differential phase  $f^{\text{M}}(x, s)$  for  $s = 1.5$ , where  $f^{\text{M}}(x, s)$  is defined in Eq. (1). The dots on  $f^{\text{M}}(x, s)$  are the discrete input data used in the reconstruction simulations, which serves as an alternative to measured wavefront difference, where the sampling intervals of them are  $\delta_x = 1$ . Below, we show the errors of reconstructed wavefronts calculated by some methods from  $f^{\text{M}}(x; s)$  by a comparison with  $\phi^{\text{True}}(x)$ . The reconstructed wavefront contains an ambiguous uniform bias, called the piston term that cannot be resolved from  $f^{\text{M}}(x; s)$  alone. Therefore, the difference is evaluated after subtracting the average of the wavefronts as

$$\Delta\phi^{\text{cal}}(x) \equiv \tilde{\phi}^{\text{cal}}(x) - \tilde{\phi}^{\text{True}}(x), \quad (47)$$

$$\tilde{\phi}(x) = \phi(x) - \bar{\phi}, \quad \bar{\phi} \equiv \langle \phi(x) \rangle, \quad (48)$$

where  $\langle \rangle$  and  $\phi^{\text{cal}}$  represent an average over  $x$  and calculated wavefront by a certain method, respectively.

Figure 2 presents the reconstructed wavefronts obtained from the simulated data using two approaches: (a) the basic method denoted as  $\phi_{s;S}(x)$ , where the spectral interpolation method coupling with natural extension method [37] was used as the basic method; and (b) the scaled method with the scale factor  $S/s$  shown in Eq. (11) employing a single integer shear, denoted as  $\phi_{s;S}^\dagger(x)$ . Reconstructions are shown for different integer shear values. The reconstructed wavefronts obtained by the basic method show that the reconstruction for  $S = 1$  which is the case of  $S < s$  exceeds the true wavefront  $\phi^{\text{True}}(x)$ , shown as black dots in Fig. 2.

Whereas the reconstructions for the cases where  $S > s$  ( $S = 2, 3$ ) underestimate  $\phi^{\text{True}}(x)$ . Comparing Eqs. (8) and (10), the main difference arises from the scaling factors of the first integral terms, which are  $1/s$  and  $1/S$ , respectively. The higher-order correction terms on the right-hand sides are also scaled by powers of  $s$  and  $S$ , leading to corresponding overestimations and underestimations in the reconstructed wavefront. Therefore, these deviations are mutually consistent and primarily governed by the difference between  $s$  and  $S$ . In contrast, the reconstructions obtained by the scaled method based on Eq. (11) exhibit close agreement with the true wavefront across all tested integer shear values. From the error perspective of  $\Delta\phi_{s;S}^\dagger(x)$ , the reconstructions for  $S = 1$  and  $S = 2$  yield nearly identical error magnitudes, whereas the reconstruction for  $S = 3$  results in a visibly larger error. This behavior is consistent with the theoretical dependence on the distance  $\epsilon = |s - S|$  between the fractional shear  $s = 1.5$  and the substituted integer shears:  $\epsilon = 0.5$  for both  $S = 1$  and  $S = 2$ , and  $\epsilon = 1.5$  for  $S = 3$ . In addition, it exhibits  $\Delta\phi_{s;2}^\dagger(x) \simeq -\Delta\phi_{s;1}^\dagger(x)$ .

Figure 3 shows the error reduction by using the proposed weighted averaging method which employs multiple scaled wavefronts. The number of employed wavefronts is represented as the superscripts,  $m$ , of  $S^m$ . Hereafter, we denote  $\phi_{s;S}^\dagger(x)$  as  $\phi_{s;S^1}^\dagger(x)$  because they are the same. As mentioned above, the errors  $\Delta\phi_{s;S^1}^\dagger(x)$  for  $S = 1$  and  $S = 2$ , exhibit opposite phases with almost the same amplitudes. Since the weights in Eq. (36) are  $w_{S^2}^{(1)} = w_{S^2}^{(2)} = 1/2$  when  $s = 1.5$ , averaging these reconstructions effectively reduces the residual error as demonstrated in  $\Delta\phi_{s;S^2}^\dagger(x)$ . Furthermore, the use of three integer shear values provides additional suppression of higher-order components, resulting in lower overall error magnitudes compared to the single-shear case.

To further investigate the error nature of the proposed algorithm, we examine the dependence of the reconstruction error on the shear value  $s$ . The reconstructed wavefronts are compared for different shear values obtained using the basic method [37] for a single shear, and the proposed weighted average method which employs one or multiple integer shears, as shown in Fig. 4. The reconstruction error,  $E_{\text{rel}}$ , is evaluated using a relative error metric, defined as

$$E_{\text{rel}}\{\phi^{\text{cal}}\} \equiv \frac{\text{RMS}\{\Delta\phi^{\text{cal}}(x)\}}{\text{RMS}\{\phi^{\text{True}}(x)\}}, \quad (49)$$

$$\text{RMS}\{a(x)\} \equiv \sqrt{\langle (a(x))^2 \rangle}, \quad (50)$$

where  $a(x)$  represents an arbitrary function. From Fig. 4, we can see that the error decreases when the fractional shear  $s$  approaches the integer shear  $S$  in all cases. The error dependencies of  $s$  of  $\phi_{s;S^m}^\dagger(x)$  for  $m = \{1, 2, 3\}$  are well fitted to linear, quadratic, and cubic functions, respectively. And the maximum errors are found at  $s = 1.5$  for  $\phi_{s;S^2}^\dagger(x)$  and  $s = 2.6$  for  $\phi_{s;S^3}^\dagger(x)$ , which are corresponding to  $\epsilon_1 = 0.5$  and  $\epsilon_2 = 0.6 \simeq 1/\sqrt{3}$ , respectively. These properties are consistent with the error estimation shown in subsections 3.1, 3.2, and 3.3.

Figure 5 summarizes the shear dependence of the reconstruction errors  $\Delta\phi_{s;S}(x)$ , and  $\Delta\phi_{s;S^m}^\dagger(x)$  for  $m = \{1, 2, 3\}$ . The integer shears,  $S$  and  $S^m$ , are selected as the nearest integer shear for each  $s$  except  $S = 0$  because

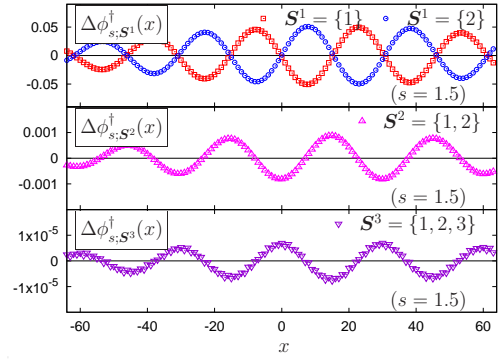


Figure 3: Errors by the weighted averaging method. The superscripts 1, 2, and 3 of  $S$  express the number of the scaled wavefronts employed in the weighted averaging method. Note: The vertical scales differ between the panels.

$\phi_{s;0}^\dagger(x)$  is identical to zero having no additional information. If  $S = 0$  is the one of the nearest integer shears, a negative shear is selected instead of  $S = 0$ ; e.g.,  $S^2 = \{-1, 1\}$  for  $s \in (0, 0.5)$ ,  $S^3 = \{-2, -1, 1\}$  for  $s \in (0, 0.5)$ ,  $S^3 = \{-1, 1, 2\}$  for  $s \in [0.5, 2)$ . In Fig. 5, the open symbols connected with a dashed line does not include the contribution of the fractional shear, the error which increases with increasing  $s$  is caused by the spectral interpolation method [37]. The contributions to the error of the fractional shear represent the difference between the dashed line and solid symbols for each  $s$ . We can find that the local maxima of errors due to the fractional shear are almost constant for each  $\phi_{s;S^m}^\dagger(x)$ . This nature is consistent with the nature shown in section 3. The exceptions are found at  $s < 1$ . This reason is that the selected integer shears  $S_q$  are not equally spaced at  $s < 1$  where the negative integer shear is selected as mentioned above.

In addition, if the norm of the normalized derivatives of  $\hat{\phi}(x)$  satisfies

$$\|\hat{\phi}^{(m-1)}(x)\| \gg \|\hat{\phi}^{(m)}(x)\| \quad (p \in \mathbb{N}), \quad (51)$$

$$\|\hat{\phi}^{(m)}(x)\| \equiv \left( \int |\hat{\phi}^{(m)}(x)|^2 dx \right)^{1/2}, \quad (52)$$

we can estimate amount of error for each method from Eqs. (28), (34) and (39). The RMSs, which are proportional to the norms, of derivatives  $\phi^{(m)}(x) = s^m \hat{\phi}^{(m)}(x)$  evaluated numerically were 0.58, 0.12, 0.024, 0.0049 for  $m = 0, 1, 2, 3$ , respectively, where the ratio between the norms of the adjacent order of differentials is 0.21 which almost equals  $k_0$ . Thus, the model shown in Eq. (46) satisfies Eq. (51) where  $s \ll L$ . Under this condition, the dominant error of  $\phi_{s;S^m}^\dagger(x)$  is induced by  $\hat{A}_m(x)$ . Moreover, the approximation  $\hat{A}_m^*(x) \approx \hat{A}_m(x)$  holds; and the dominant term of  $\hat{A}_m(x)$  is determined by the minimum derivative of  $\hat{\phi}(x)$  as

$$\hat{A}_m(x) \sim \alpha_{1,m}^* \hat{\phi}^{(m)}(x). \quad (53)$$

Therefore, the theoretical relative error in the weighted av-

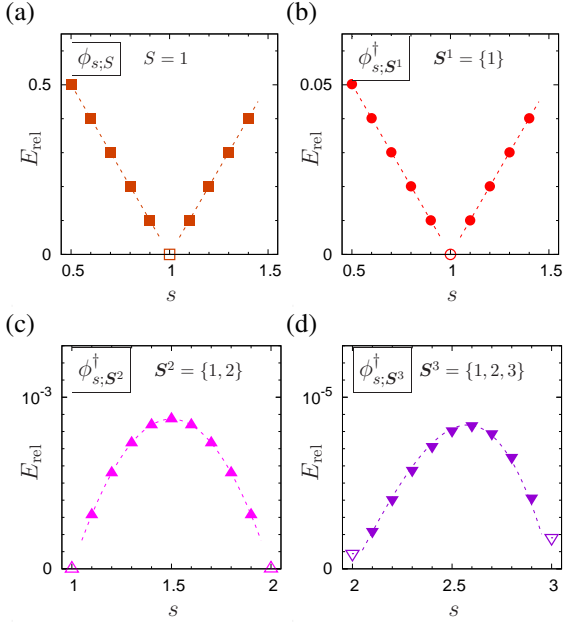


Figure 4: Shear dependence of relative reconstruction errors. (a) Reconstructed wavefront using the basic method. (b)-(d) Reconstructed wavefronts evaluated by the proposed method using single, two and three integer shear values, respectively. Open and solid symbols denote integer and fractional shears, respectively. The dashed lines in subfigures represent the theoretical error obtained by least-squares fitting for solid points with linear, quadratic, or cubic functions. The scales of vertical axes differ between subfigures. The interval between evaluations for  $s$  is  $\delta_x/10$ .

eraging methods is

$$\tilde{E}_{\text{rel}} \left\{ \phi_{s;S^m}^\dagger \right\} \sim |\alpha_{1,m}^*| \mathcal{E}_{\text{max}}^m \frac{\text{RMS}\{\phi^{(m)}(x)\}}{\text{RMS}\{\phi^{(0)}(x)\}}, \quad (54)$$

$$\mathcal{E}_{\text{max}}^m = \max_s \left\{ \left| \prod_{i=1}^m \epsilon_i \right| \right\}. \quad (55)$$

From the definition of  $\alpha_{l,m}^*$  shown in Eq. (19)  $\alpha_{1,m}^* = \{1/4, 1/12, 1/144\}$  is obtained. The factor of  $\mathcal{E}_{\text{max}}^m$  can be estimated from the local maxima of the products in Eqs. (37) and (45); i.e.,  $|\epsilon| = \delta_x/2$  for  $\phi_{s;S^1}^\dagger(x)$ ,  $\phi_{s;S^2}^\dagger(x)$  and  $\epsilon = \delta_x/\sqrt{3}$  for  $\phi_{s;S^3}^\dagger(x)$ ; and the results are  $\mathcal{E}_{\text{max}}^m = \{\delta_x/2, \delta_x^2/4, 2\delta_x^3/(3\sqrt{3})\}$ . The theoretical errors are estimated from these quantities as  $\tilde{E}_{\text{rel}} \left\{ \phi_{s;S^m} \right\} = \{0.050, 0.00086, 2.3 \times 10^{-5}\}$  for  $m = \{1, 2, 3\}$ , respectively. For comparisons, the actual relative errors for the result shown in Fig.5 were  $E_{\text{rel}} \left\{ \phi_{s;S^m}^\dagger(x) \right\} \simeq \{0.050, 0.00088, 0.81 \times 10^{-5}\}$  around  $s \simeq 2.5$ , which agree with the theoretical ones for  $S^1$  and  $S^2$ , and the order is the same for  $S^3$  in which the error for the integer shear is comparative.

In this section, we demonstrated that the errors of  $\phi_{s;S^m}^\dagger(x)$  are, qualitatively and quantitatively, consistent with the theory shown in section 3. However, the readers may wonder whether this result was due to the fact that the phase model shown in Eq. (46) just happens to satisfy Eq. (51). The validity of Eq. (51) follows from the spectral characteristics of  $\hat{\phi}(x)$ . Since the derivative in the Fourier domain is weighted by  $|k|$ , if the reconstructed wavefront is sufficiently smooth; i.e., the Fourier spectrum of  $\hat{\phi}(x)$  is effectively limited as  $|k| \lesssim k_{\text{max}}$ , the norm of the  $m$ -th

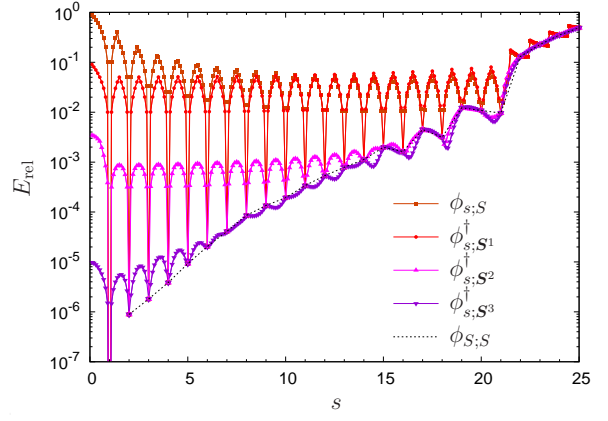


Figure 5: Shear dependence of relative errors. The open symbols at the local minima and solid symbols represent the case where  $s$  are integer shears and fractional shears, respectively.

derivative of  $\hat{\phi}(x)$  satisfies

$$\left\| \hat{\phi}^{(m+1)}(x) \right\| \lesssim s k_{\text{max}} \left\| \hat{\phi}^{(m)}(x) \right\|. \quad (56)$$

The effective limit of the model shown in Eq. (46) was  $k_{\text{max}} \simeq k_0$ , which is a result from the convolution theorem in which the peaks represented by a Dirac's delta function,  $\delta(k \pm k_0)$ , in the spectral domain are blurred by the narrow Gaussian function with the spectral width  $1/w$ . And this model satisfies Eq. (51) as mentioned above. In the case of a more practical model such as a superposition of several Gaussian functions with the minimum width  $w_{\text{min}}$  without cosine modulation ( $k_0 = 0$ ), the effective limit  $k_{\text{max}}$  is determined only from the spectral width of the Gaussian functions as  $k_{\text{max}} \approx 1/w_{\text{min}}$ . This suggests that the condition of Eq. (51) is met even when  $s$  is larger, since  $k_{\text{max}}$  is smaller than the cosine modulated model. Consequently, it can be concluded that the condition to reduce the error due to the fractional shear is

$$s k_{\text{max}} \ll 1, \quad (57)$$

and the weighted averaging method is applicable for models without steep changing distribution such as step-shaped phase distributions.

## 5. Conclusion

Wavefront reconstruction in lateral shearing interferometry is often hindered by the practical difficulty of realizing shears that are integer multiples of the detector sampling interval. Conventional methods that approximate fractional shears by the nearest integer introduce systematic reconstruction errors, which can become significant in precision applications. In this work, we proposed a weighted integer shear averaging method that systematically reduces these errors by combining reconstructions from multiple nearby integer shears with analytically chosen weights. Theoretical error analysis demonstrated that two-shear averaging cancels first-order error terms, while three-shear averaging further suppresses second-order contributions. Numerical simulations confirmed these predictions, showing that the proposed method achieves substantially lower RMS error than conventional single-shear reconstruction. The approach is computationally efficient, requires no changes

to existing shear interferometer hardware, and can be naturally extended to two-dimensional cases by cooperating with the other method to solve the piston term problem. Overall, the results indicate that weighted integer shear averaging provides a practical and accurate strategy for wavefront reconstruction under fractional shear conditions.

## Acknowledgements

This research was supported by Japan Society for the Promotion of Science (JSPS), 22K04117.

## References

- [1] T. Yoshizawa (Ed.), *Handbook of Optical Metrology: Principles and Applications*, 2nd Edition, CRC Press, 2015.
- [2] R. S. Sirohi, *Introduction to Optical Metrology*, 2nd Edition, Taylor & Francis, 2009.
- [3] U. Schnars, C. Falldorf, J. Watson, W. Jüptner, *Digital Holography and Wavefront Sensing: Principles, Techniques and Applications*, Springer, 2015.
- [4] G. Mana, E. Massa, C. P. S. Sasso, Wavefront errors in a two-beam interferometer, *Metrologia* 55 (4) (2018) 535–540. doi:10.1088/1681-7575/aacae6.
- [5] S. Zhang, Z. Xu, B. Chen, L. Yan, J. Xie, The comparison of environmental effects on michelson and fabry–perot interferometers utilized for the displacement measurement, *Sensors* 10 (4) (2011) 2577–2593. doi:10.3390/s100402577.
- [6] P. Bon, G. Maucort, B. Wattellier, S. Monneret, Quadriwave lateral shearing interferometry for quantitative phase microscopy of living cells, *Opt. Express* 17 (15) (2009) 13080–13094. doi:10.1364/OE.17.013080.
- [7] S. Tomioka, S. Nishiyama, S. Heshmat, Y. Hashimoto, K. Kurita, Three-dimensional gas temperature measurements by computed tomography with incident angle variable interferometer, in: C. A. Bouman, K. D. Sauer (Eds.), *Computational Imaging XIII*, Vol. 9401, International Society for Optics and Photonics, SPIE, 2015, p. 94010J. doi:10.1117/12.2082499.
- [8] S. Tomioka, S. Nishiyama, N. Miyamoto, D. Kando, S. Heshmat, Weighted reconstruction of three-dimensional refractive index in interferometric tomography, *Appl. Opt.* 56 (24) (2017) 6755–6764. doi:10.1364/AO.56.006755.
- [9] T. Ling, J. Jiang, R. Zhang, Y. Yang, Quadriwave lateral shearing interferometric microscopy with wide-band sensitivity enhancement for quantitative phase imaging in real time, *Scientific reports* 7 (1) (2017) 1–14. doi:10.1038/s41598-017-00053-7.
- [10] M. V. R. K. Murty, The use of a single plane parallel plate as a lateral shearing interferometer with a visible gas laser source, *Appl. Opt.* 3 (4) (1964) 531–534. doi:10.1364/AO.3.000531.
- [11] M. E. Riley, M. A. Gusinow, Laser beam divergence utilizing a lateral shearing interferometer, *Appl. Opt.* 16 (10) (1977) 2753–2756. doi:10.1364/AO.16.002753.
- [12] M. P. Rimmer, J. C. Wyant, Evaluation of large aberrations using a lateral-shear interferometer having variable shear, *Appl. Opt.* 14 (1) (1975) 142–150. doi:10.1364/AO.14.000142.
- [13] G. Harbers, P. J. Kunst, G. W. R. Leibbrandt, Analysis of lateral shearing interferograms by use of zernike polynomials, *Appl. Opt.* 35 (31) (1996) 6162–6172. doi:10.1364/AO.35.006162.
- [14] S. Okuda, T. Nomura, K. Kamiya, H. Miyashiro, K. Yoshikawa, H. Tashiro, High-precision analysis of a lateral shearing interferogram by use of the integration method and polynomials, *Appl. Opt.* 39 (28) (2000) 5179–5186. doi:10.1364/AO.39.005179.
- [15] F. Dai, F. Tang, X. Wang, O. Sasaki, M. Zhang, High spatial resolution zonal wavefront reconstruction with improved initial value determination scheme for lateral shearing interferometry, *Appl. Opt.* 52 (17) (2013) 3946–3956. doi:10.1364/AO.52.003946.
- [16] I. Mochi, K. A. Goldberg, Modal wavefront reconstruction from its gradient, *Appl. Opt.* 54 (12) (2015) 3780–3785. doi:10.1364/AO.54.003780.
- [17] T. Ling, Y. Yang, D. Liu, X. Yue, J. Jiang, J. Bai, Y. Shen, General measurement of optical system aberrations with a continuously variable lateral shear ratio by a randomly encoded hybrid grating, *Appl. Opt.* 54 (30) (2015) 8913–8920. doi:10.1364/AO.54.008913.
- [18] R. Shi, H. Liu, Y. Shao, J. Bai, Wavefront reconstruction for double-grating ronchi lateral shearing interferometry with nonlinear optimization, in: *SPIE Optical Design and Testing XIII (Proceedings of SPIE Vol. 12765)*, 2023, p. 127650S. doi:10.1117/12.2688489.
- [19] Y. Luo, Z. Luo, D. Hou, D. Bian, Y. He, W. Jiang, Y. Li, High-flexibility single-shot wavefront measurement with dual-lateral shearing interferometry, *Optics and Lasers in Engineering* 186 (2025) 108792. doi:10.1016/j.optlaseng.2024.108792.
- [20] W. Southwell, Wave-front estimation from wave-front slope measurements, *J. Opt. Soc. Am.* 70 (8) (1980) 998–1006. doi:10.1364/JOSA.70.000998.
- [21] W. Zou, Z. Zhang, Generalized wave-front reconstruction algorithm applied in a shack–hartmann test, *Appl. Opt.* 39 (2) (2000) 250–268. doi:10.1364/AO.39.000250.

- [22] F. Dai, F. Tang, X. Wang, O. Sasaki, Generalized zonal wavefront reconstruction for high spatial resolution in lateral shearing interferometry, *J. Opt. Soc. Am. A* 29 (9) (2012) 2038–2047. doi:10.1364/JOSAA.29.002038.
- [23] F. Dai, J. Li, X. Wang, Y. Bu, Exact two-dimensional zonal wavefront reconstruction with high spatial resolution in lateral shearing interferometry, *Optics Communications* 367 (2016) 264 – 273. doi:10.1016/j.optcom.2016.01.068.
- [24] D. Zhai, S. Chen, S. Xue, Z. Yin, Exact recovery of wavefront from multishearing interferograms in spatial domain, *Appl. Opt.* 55 (28) (2016) 8063–8069. doi:10.1364/AO.55.008063.
- [25] R. H. Hudgin, Wave-front reconstruction for compensated imaging, *J. Opt. Soc. Am.* 67 (3) (1977) 375–378. doi:10.1364/JOSA.67.000375.
- [26] K. R. Freischlad, C. L. Koliopoulos, Modal estimation of a wave front from difference measurements using the discrete fourier transform, *J. Opt. Soc. Am. A* 3 (11) (1986) 1852–1861. doi:10.1364/JOSAA.3.001852.
- [27] M. Servin, D. Malacara, J. L. Marroquin, Wavefront recovery from two orthogonal sheared interferograms, *Appl. Opt.* 35 (22) (1996) 4343–4348. doi:10.1364/AO.35.004343.
- [28] Y. feng Guo, H. Chen, J. Xu, J. Ding, Two-dimensional wavefront reconstruction from lateral multi-shear interferograms, *Opt. Express* 20 (14) (2012) 15723–15733. doi:10.1364/OE.20.015723.
- [29] Y. Guo, J. Xia, J. Ding, Recovery of wavefront from multi-shear interferograms with different tilts, *Opt. Express* 22 (10) (2014) 11407–11416. doi:10.1364/OE.22.011407.
- [30] C. Elster, I. Weingärtner, Solution to the shearing problem, *Appl. Opt.* 38 (23) (1999) 5024–5031. doi:10.1364/AO.38.005024.
- [31] C. Elster, I. Weingärtner, Exact wave-front reconstruction from two lateral shearing interferograms, *J. Opt. Soc. Am. A* 16 (9) (1999) 2281–2285. doi:10.1364/JOSAA.16.002281.
- [32] C. Elster, Exact two-dimensional wave-front reconstruction from lateral shearing interferograms with large shears, *Appl. Opt.* 39 (29) (2000) 5353–5359. doi:10.1364/AO.39.005353.
- [33] A. Dubra, C. Paterson, C. Dainty, Wave-front reconstruction from shear phase maps by use of the discrete fourier transform, *Appl. Opt.* 43 (5) (2004) 1108–1113. doi:10.1364/AO.43.001108.
- [34] C. Falldorf, Y. Heimbach, C. von Kopylow, W. Jüptner, Efficient reconstruction of spatially limited phase distributions from their sheared representation, *Appl. Opt.* 46 (22) (2007) 5038–5043. doi:10.1364/AO.46.005038.
- [35] D. Zhai, S. Chen, F. Shi, High spatial resolution zonal reconstruction with modified multishear method in frequency domain, *Appl. Opt.* 56 (29) (2017) 8067–8074. doi:10.1364/AO.56.008067.
- [36] D. Zhai, S. Chen, F. Shi, Z. Yin, Exact multi-shear reconstruction method with different tilts in spatial domain, *Optics Communications* 402 (2017) 453 – 461. doi:10.1016/j.optcom.2017.06.031.
- [37] S. Tomioka, N. Miyamoto, Y. Yamauchi, Y. Matsumoto, S. Heshmat, Wavefront restoration from lateral shearing data using spectral interpolation, *Appl. Opt.* 62 (29) (2023) 7549–7559. doi:10.1364/AO.500453.
- [38] X. Tian, M. Itoh, T. Yatagai, Simple algorithm for large-grid phase reconstruction of lateral-shearing interferometry, *Appl. Opt.* 34 (31) (1995) 7213–7220. doi:10.1364/AO.34.007213.
- [39] M. Takeda, H. Ina, S. Kobayashi, Fourier-transform method of fringe-pattern analysis for computer-based topography and interferometry, *J. Opt. Soc. Am.* 72 (1) (1982) 156–160. doi:10.1364/JOSA.72.000156.
- [40] S. Tomioka, S. Nishiyama, Phase unwrapping for noisy phase map using localized compensator, *Appl. Opt.* 51 (21) (2012) 4984–4994. doi:10.1364/AO.51.004984.
- [41] S. Heshmat, S. Tomioka, S. Nishiyama, A. Hirokami, Localized compensator phase unwrapping algorithm based on flux conservable solver, *Journal of Computational Science* 62 (2022) 101752. doi:10.1016/j.jocs.2022.101752.